Spray Pyrolysis Deposition of ZnFe$_2$O$_4$/Fe$_2$O$_3$ Composite Thin Films on Hierarchical 3-D Nanospikes for Efficient Photoelectrochemical Oxidation of Water

Shabeeb Hussain,[†] Shazia Hussain,[†] Aashir Waleed,[‡,§] Mohammad Mahdi Tavakoli,[‡,∥] Shihe Yang,[⊥] Muhammad Khawar Rauf,[†] Zhiyong Fan,*,[‡] and Muhammad Arif Nadeem*,[†]

[†]Catalysis and Nanomaterials Lab 27, Department of Chemistry, Quaid-i-Azam University, Islamabad 4533, Pakistan
[‡]Department of Electronic and Computer Engineering and [⊥]Department of Chemistry, William Mong Institute of Nano Science and Technology, The Hong Kong University of Science and Technology, Clear Water Bay, Kowloon, Hong Kong SAR, China
[§]Department of Electrical Engineering, University of Engineering and Technology, Lahore (FSD Campus), 3.5 km, Khurrianwala-Makuana Bypass, Faisalabad 38000, Pakistan
[∥]Department of Materials Science and Engineering, Sharif University of Technology, Azadi Street, 113659466 Tehran, Iran

S *Supporting Information*

ABSTRACT: In this work, we study the role of nanotextured ZnFe$_2$O$_4$/Fe$_2$O$_3$ composite thin films fabricated by ultrasonic spray pyrolysis (USP) on the photoelectrochemical water oxidation reactions. The ZnFe$_2$O$_4$/Fe$_2$O$_3$ composites with different molar ratios are deposited on three-dimensional nanospikes (NSP) substrate, and the results are compared with those for planar devices. It is observed that optical absorption and charge separation due to larger surface area is significantly enhanced in nanotextured photoactive ZnFe$_2$O$_4$/Fe$_2$O$_3$ films. After characterization of ZnFe$_2$O$_4$/Fe$_2$O$_3$ composite films with different molar ratios (ZF1, ZF2, and ZF3), we find that the nanotextured ZF1 composite with a molar ratio of 1:1 has the highest activity with photocurrent density of 2.19 mA/cm^2 in photoelectrochemical oxidation of water. This photocurrent density is 3.4 and 2.73 times higher than the photocurrent density values of pure hematite on planar fluorine-doped tin oxide (FTO) coated glass and the highest reported value of ZnFe$_2$O$_4$/Fe$_2$O$_3$ composite, respectively. In addition, the results of electrochemical impedance spectroscopy (EIS) and photoluminescence (PL) tests indicate lower charge transfer resistance and faster charge extraction for the nanotextured ZnFe$_2$O$_4$/Fe$_2$O$_3$ composite (ZF1). Overall, our new fabrication process for the ZnFe$_2$O$_4$/Fe$_2$O$_3$ composite together with the effect of nanostructured substrate shows a better charge separation and enhanced optical absorption, resulting in a highly efficient photoelectrochemical water-splitting device.
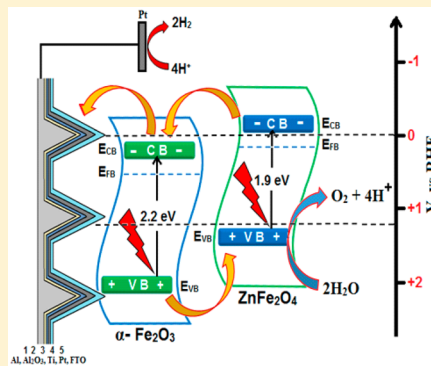
■ INTRODUCTION

Photoelectrochemical (PEC) splitting of water is the paramount process to obtain chemical energy from a clean, economic, and sustainable source.[1−6] In a PEC cell, the incident light is absorbed by a photoelectrode, which generates an electron and hole pair after excitation of electrons from the valence band to the conduction band. These photogenerated electrons and holes are responsible for the splitting of water into hydrogen and oxygen molecules.[7] The key features of semiconductor materials for water-splitting application are (1) the ability to generate sufficient voltage upon irradiation for oxidation or reduction of water, (2) an ideal band gap to absorb maximum solar radiation, (3) alignment of band levels in semiconductor materials with redox potentials of hydrogen and oxygen, and (4) sufficient diffusion lengths of photogenerated electrons and holes to move from the bulk to the surface of semiconductor material that is in contact with the electrolyte and outer circuit.[8] Currently, massive efforts have been

performed by scientists to discover new materials that can fulfill the maximum required criteria for efficient PEC water splitting.[9−12] Among these materials, hematite (α-Fe$_2$O$_3$) is studied extensively due to its suitable optical band gap.[13−15] However, several factors have limited the performance of hematite in PEC water oxidation such as low absorption coefficient at the wavelength of 550 nm, low carrier mobility, and short diffusion length.[2,16] To tackle these problems, research employed a doping technique using various elements such as Ti, Si, Pt, and Zn to adjust the hematite electronic structure and enhance carrier mobility.[17,18] Hematite doped with zinc shows the best results due to the superior characteristics of zinc ferrite (ZnFe$_2$O$_4$) over pure hematite, including excellent electric and magnetic properties and good

sensitivity in visible light.[19−21] In addition, $ZnFe_2O_4$ is stable in alkaline as well as in weak acidic medias.[22] And its narrow band gap (1.9 eV) and ideal band levels make it an ideal candidate for fabrication of a heterojunction structure with α-Fe_2O_3. In fact, the conduction and valence bands of $ZnFe_2O_4$ are more negative than α-Fe_2O_3, which helps for better separation of photogenerated electron−hole pairs in the $ZnFe_2O_4$/α-Fe_2O_3 composite.[23] In this regard, some research groups have employed this composite as an active layer for the water-splitting application. McDonald et al. treated and modified the surface of α-Fe_2O_3 nanoparticles by immersing the electrode in a solution containing Zn^{2+} ions, resulting in formation of a $ZnFe_2O_4$ shell on the surface of hematite and enhancement of the photocurrent response compared with the case for the pure α-Fe_2O_3 electrode.[22] Miao et al. employed the $ZnFe_2O_4$/Fe_2O_3 composite as the photoanode, and after doping hematite with Ti, they were able to enhance the photocurrent response of the device up to 0.15 mA/cm².[23] Nowadays, researchers have paid attention to the photoanode structures to solve the diffusion length problem of photogenerated holes. It is worthwhile to point out that the nanotextured photoanodes enhance the light absorption and carrier collection, due to the larger surface area.[2] For instance, Liu et al. fabricated a nanorod array of α-Fe_2O_3 covered with a thin film of $ZnFe_2O_4$, which results in the formation of $ZnFe_2O_4$/α-Fe_2O_3 heterojunctions with an enhanced current density of 0.29 mA/cm².[24] In addition, Luo et al. recently designed and synthesized a highly oriented nanocolumnar heterojunction structure of α-Fe_2O_3/$ZnFe_2O_4$ using the atomic layer deposition technique. They have reported a photocurrent density of 0.8 mA/cm² at 1.23 V vs RHE using this structure, which is higher than all previously reported Fe_2O_3/$ZnFe_2O_4$ heterostructured photoanodes.[25]

Herein, we report the fabrication of $ZnFe_2O_4$/α-Fe_2O_3 composite thin films with different molar ratios on planar (P) fluorine-doped tin oxide (FTO) as well as 3-D nanostructured substrate (NSP) using the ultrasonic spray pyrolysis (USP) process for PEC water-splitting application. We find that the composite ZF1 with a molar ratio of 1:1 for $ZnFe_2O_4$ and α-Fe_2O_3 shows a drastically high photocurrent density of 1.14 and 2.19 mA/cm² at 1.23 V_{RHE} for planar and NSP samples, respectively, which are 1.8 and 3.4 times higher than that for pure hematite on FTO glass, respectively. This high photocurrent density for the NSP sample is due to its higher surface area resulting in better optical absorption and carrier collection; moreover, these results are in good agreement with the results of electrochemical impedance spectroscopy (EIS) and photoluminescence (PL) tests.

The band diagram of the $ZnFe_2O_4$/α-Fe_2O_3 composite device based on NSP is illustrated in Scheme 1. The Fermi level of α-Fe_2O_3 is 0.18 eV lower than that of $ZnFe_2O_4$.[24,26] The reported values of band gaps for $ZnFe_2O_4$ and α-Fe_2O_3 are 1.9 and 2.2 eV, respectively.[24] As illustrated in Scheme 1, the band alignment of $ZnFe_2O_4$ and α-Fe_2O_3 allows the flow of photogenerated electrons and holes at their interface, leading to a better charge separation and lower carrier recombination. Table 1 shows the results of our device based on NSP compared with the previous reports on $ZnFe_2O_4$/α-Fe_2O_3 composite for the water-splitting device.

■ EXPERIMENTAL SETUP

Fabrication of 3D NSP. The highly ordered 3D nanospikes on the polished surface of aluminum foil were fabricated according to our previous publication.[27] Briefly, aluminum foil

Scheme 1. Schematic Representation of Energy Band Positions of $ZnFe_2O_4$ and α-Fe_2O_3 Dual-Absorber System
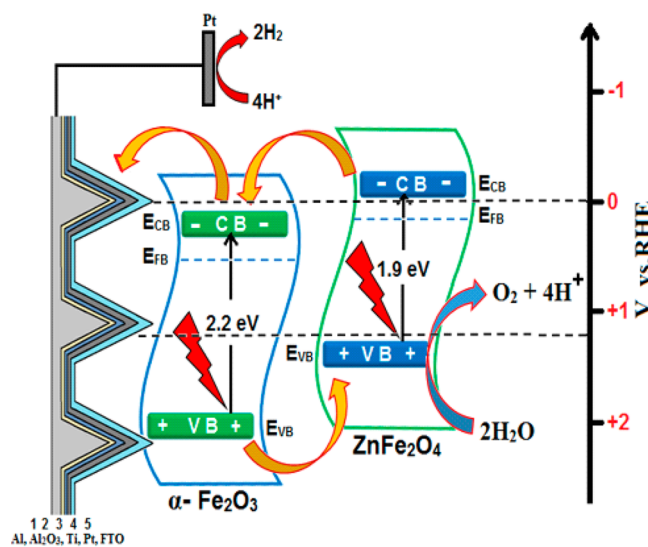
was cut into small rectangular pieces with the size of 1.5 × 2.5 cm² and flattened by pressing between two glass slides.[28,29] The flattened chips of aluminum were sonicated in 2-propanol for 10 min followed by rinsing with deionized water and acetone. The cleaned chips of aluminum were dried with compressed air, followed by polishing in a 1:3 (v/v) solution of $HClO_4$ and ethanol. The applied voltage was 12 V for 2 min at 10 °C. The polished aluminum chips were again rinsed with DI-water and dried. To grow an anodized aluminum oxide (AAO) layer, polished aluminum chips were imprinted by a square mold consisting of ordered nanopillars array with 200 nm height and 1.2 μm pitch. The applied pressure was 2×10^4 N cm^{-2} on the silicon mold for 5 s. To fabricate an AAO film, 480 V was applied in a solution containing of 9 mL of 0.1% (w/w) phosphoric acid, 240 mL of 1:1 (v/v) ethylenediamine, and a 2% (w/w) aqueous solution of citric acid. The anodization process was performed for 6 h at 10 °C. After the anodization process, the chips were washed with DI-water and dried. To make the well-ordered 3D nanospikes, the as grown AAO layer was removed by etching with a solution of 1.5% (w/w) of chromic acid and 6% (w/w) of phosphoric acid in water at 98 °C for 60 min. Then, a thin layer of AAO on 3D NSP was grown to protect the surface against basic electrolytes. In this case, a low potential anodization was done at 20 V for 2 h in a solution of 3.4 wt % of sulfuric acid in water.

Deposition of Ti and Pt Protective Layer. As aluminum is highly reactive in aqueous NaOH solution (used for PEC measurements), nanospike substrates were protected by deposition of a 100 nm thick layer of Ti followed by a 50 nm thick layer of platinum using the magnetron sputtering technique.

Deposition of Fluorine Doped Tin Oxide (FTO). A thin layer of fluorine-doped tin oxide (FTO) was deposited on the top of platinum layer covering 3D nanospikes by using the ultrasonic spray pyrolysis (USP) technique. An ethanoic solution of 0.2 M $SnCl_4$ and 0.04 M of NH_4F was prepared for deposition of FTO film. Compressed air was used as the carrier gas, and the flow rate was controlled accordingly. The growth temperature of the FTO film was fixed at 450 °C.

Deposition of $ZnFe_2O_4$/α-Fe_2O_3 on 3D NSP. Thin films of the $ZnFe_2O_4$/α-Fe_2O_3 composite with different molar ratios

Table 1. Results of our PCE Device Compared with the Literature

molar ratio	photocurrent density at 1.23 V_{RHE} (mA/cm^2)	illumination intensity	electrolyte condition	PH	ref
1:1	0.05	AM1.5G illumination (100 mW cm^{-2}).	1 M NaOH	13.6	23
1:1	0.25	AM1.5G illumination (100 mW cm^{-2}).	1 M NaOH	13.6	24
not known	0.3	AM1.5G illumination (100 mW cm^{-2}).	1 M NaOH	13.6	25
not known	0.8	AM1.5G illumination (100 mW cm^{-2}).	1 M KOH	13.6	26
1:1	1.14	AM1.5G illumination (100 mW cm^{-2}).	1 M NaOH	13.6	current work

were deposited on FTO-coated NSP samples as well as planar ones. Solutions containing $FeCl_3 \cdot 6H_2O$ and $ZnCl_2 \cdot 2H_2O$ with different molar ratios were dissolved in ethanol and used as precursors for deposition of the composite film. Sodium citrate was added to the above solutions as a complexing agent, which facilitates the easy evaporation of metallic ions during the USP process. The molar concentrations of $FeCl_3 \cdot 6H_2O$ and $ZnCl_2 \cdot 2H_2O$ in the precursor solutions and the composition of the composite thin film are given in Table S1. The USP process was performed for 10 min at 450 °C, followed by annealing at 500 °C in a tubular furnace for 3 h in ambient air.

Deposition of $ZnFe_2O_4/\alpha$-Fe_2O_3 on FTO Glass. FTO-coated glasses were cut in pieces of 1.5 × 2.5 cm^2, sonicated in 2-propanol for 10 min, rinsed with acetone and then DI-water, and dried by compressed air.[30] A small portion of FTO-coated glass was covered with aluminum foil for contact. The composite thin films of $ZnFe_2O_4/\alpha$-Fe_2O_3 were deposited by the USP technique using the same precursor solution as explained in Table S1. The samples were annealed for 3 h in ambient air. After annealing, the samples were slowly cooled to avoid any crack nucleation.

Electrode Preparation. With silver paste, the copper wires were connected with the FTO-coated region of the glass, which was protected by aluminum foil from the photoactive composite layer. The electrodes were then covered by insulator silicon paste to avoid any contact of the electrolyte solution with the copper wire or the exposed FTO coating of the glass. An area of 1 cm^2 consisting of $ZnFe_2O_4/\alpha$-Fe_2O_3 composite thin film on the top was left uncovered for photoelectrochemical reaction. The electrodes of 3D samples were also prepared by following a similar process with the exception that the other side was completely covered by insulating silicon paste to avoid any contact of the electrolyte solution with the bare aluminum surface.

Photoelectrochemical Measurements. The photoelectrochemical water oxidation on $ZnFe_2O_4/\alpha$-Fe_2O_3 composite thin films was investigated as a function of the ratio between $ZnFe_2O_4$ and α-Fe_2O_3. The samples were tested in one compartment cell consisting of a three-electrode system in a 1 M NaOH solution in water. The fabricated electrodes were used as the working electrode, and Ag/AgCl (4 M KCl) and platinum foil were used as a reference and counter electrode, respectively. The surface of the working electrodes was exposed to light using a sun simulator (AM 1.5, 100 mW/cm^2) and photocurrent densities were measured from −0.4 to +0.8 V (vs Ag/AgCl) using linear sweep voltammetry (LSV) with a scan rate of 50 mV/s. The potential values vs Ag/AgCl were then converted into reversible hydrogen electrode (RHE) using the Nernst equation ($E_{RHE} = E_{Ag+AgCl} + 0.059pH + E°_{Ag/AgCl}$).

PHOTOLUMINESCENCE STUDIES

The steady state photoluminescence analyses were carried out by using a FLS920P flourescence spectrometer.

ELECTROCHEMICAL IMPEDANCE MEASUREMENTS

For charge transfer studies, we used an Eco Chemie Auto lab PGSTAT 12 potentiostat/galvanostat (Utrecht, The Netherlands). The EIS measurements were performed in 1 M NaOH solution under the applied voltage of 1.23 vs RHE in single compartment three electrode systems with Ag/AgCl and platinum wire as reference and counter electrodes, respectively.

RESULTS AND DISCUSSION

The crystal structure of as-deposited $ZnFe_2O_4/\alpha$-Fe_2O_3 composite films (ZF1 and ZF2) and pure Fe_2O_3 were studied by X-ray diffraction (XRD; Philips PW-1830) with Cu Kα radiation (λ = 1.5406 A), as shown in Figure 1. As seen, the
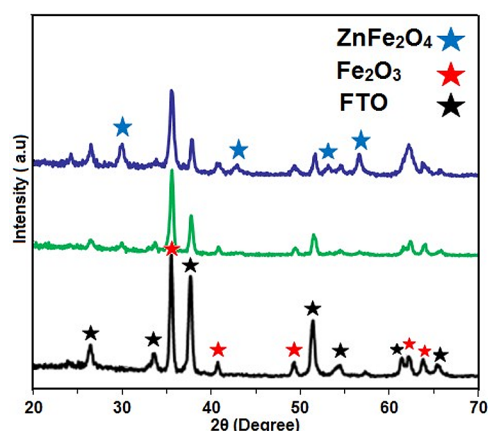

Figure 1. PXRD patterns of $ZnFe_2O_4/\alpha$-Fe_2O_3 composite ZF2 (green), ZF1 (blue), and pure Fe_2O_3 (black) deposited on FTO glass.

observed peaks of composite films corresponded to either α-Fe_2O_3 (JCPDS 33-0664) or $ZnFe_2O_4$ (JCPDS 22-1012). This indicates that the diffraction patterns of ZF1 and ZF2 composites are well-matched with the standard diffraction pattern of rhombohedral α-Fe_2O_3 (JCPDS 33-0664) and the spinel structure of $ZnFe_2O_4$ (JCPDS 22-1012). The XRD peaks located at 2θ = 29.93, 35.45, 36.83, 42.89, 53.09, 56.57, and 62.15° are ascribed to 220, 311, 222, 400, 422, 511, and 440 planes of spinel $ZnFe_2O_4$, while the peaks appeared at 2θ = 24.17, 35.74, 40.91, 49.49, 62.4 and 64.0° are correspond to 012, 110, 113, 024, 214 and 300 planes of the rhombohedral α-Fe_2O_3. The absence of diffraction peaks of ZnO (JCPDS 5-0664) in XRD spectra of both ZF1 and ZF2 composites depicts that the Zn atom is only presented in the form of $ZnFe_2O_4$.

To further study the valence state and chemical composition of the $ZnFe_2O_4/\alpha$-Fe_2O_3 composites, X-ray photoelectronic spectroscopy (XPS) was employed. It is verified from full scan XPS spectra of ZF1 and ZF2 composites (Figure 2A) that Zn, Fe, and O are the main elements of these composite films. The carbon peak at the binding energy 285.2 eV is ascribed to the
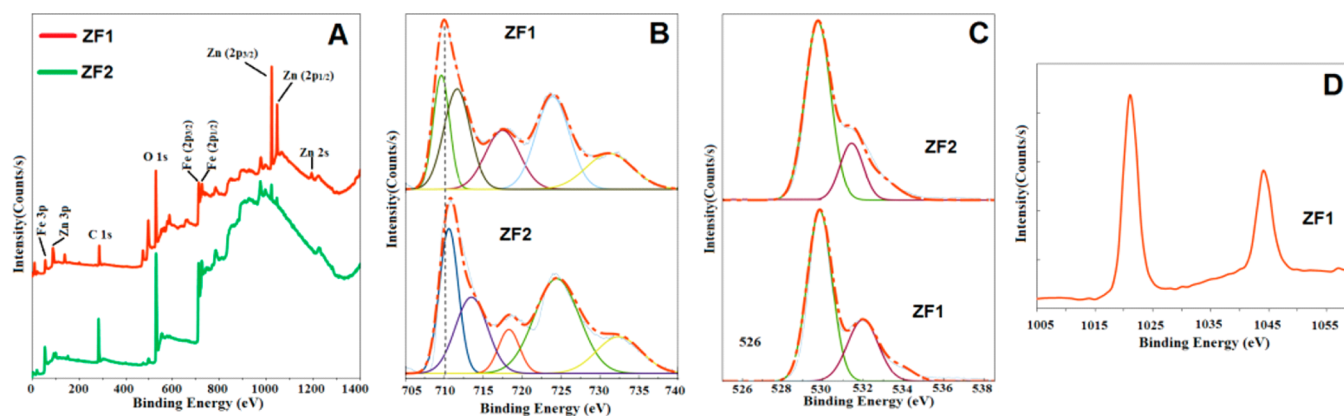
Figure 2. (A) Full XPS spectra of composite ZF2 (green) and ZF1 (blue), (B) Fe 2p scan of ZF-2 (green) and ZF1 (blue), (C) O 1s scan of CZF2 (green) and ZF1 (blue), and (D) Zn 2p scan of ZF1.
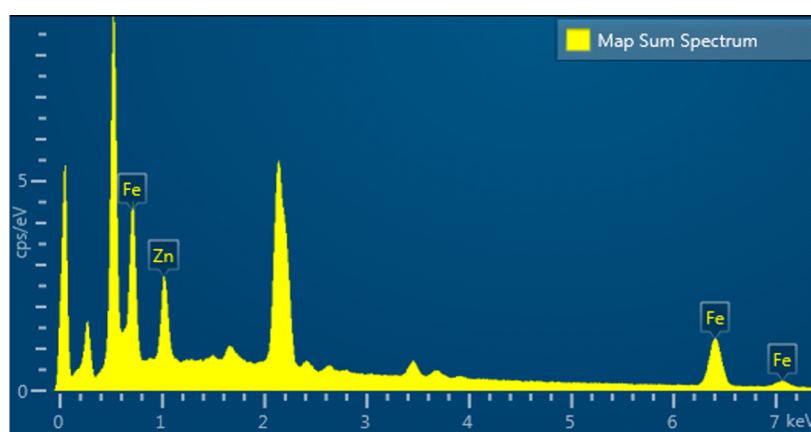
Figure 3. XRF spectrum of ZnFe2O4/α-Fe2O3 composites, ZF1.
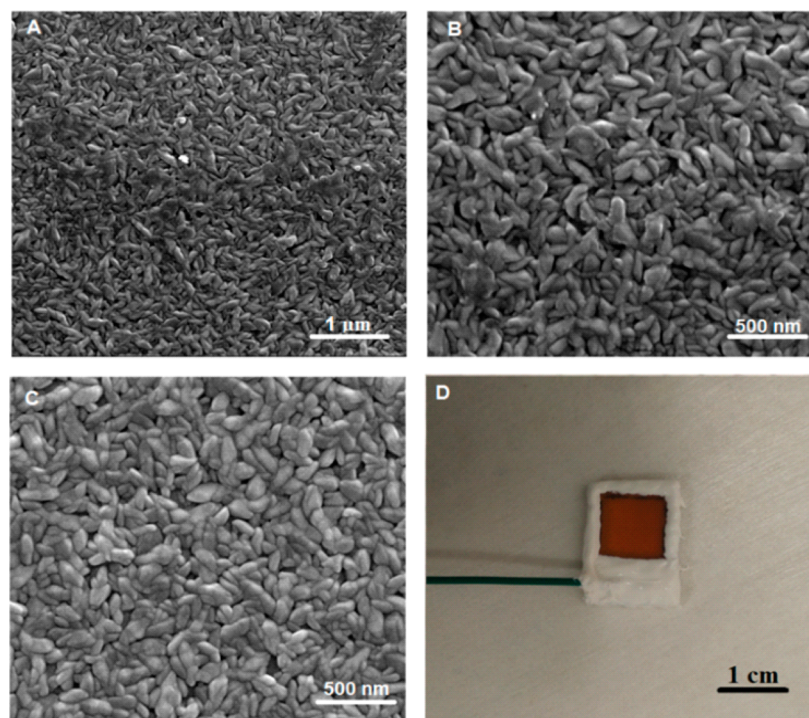
Figure 4. (A) Low-magnification SEM images of $ZnFe_2O_4/\alpha$-Fe_2O_3 composite (ZF2). (B) and (C) High-magnification SEM images of $ZnFe_2O_4/\alpha$-Fe_2O_3 thin film on FTO glass. (D) Optical photograph of the planar electrode.
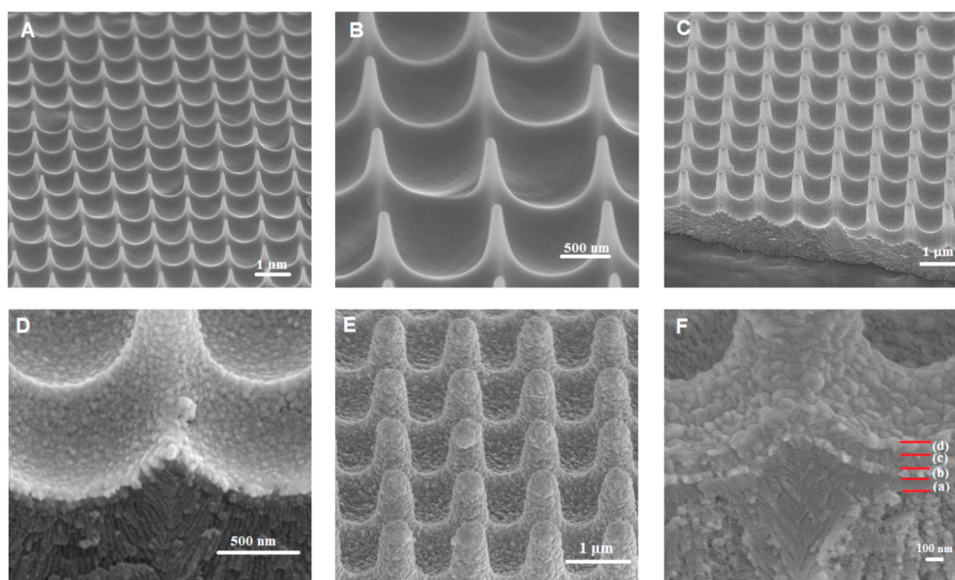
Figure 5. Low (A) and high-magnification (B) SEM image of ordered 3D nanospikes, (C) SEM image of nanospikes covered by Ti and Pt protective thin films, (D) high-resolution SEM image showing protective Ti and Pt film deposited on the top, (E) SEM image of final device showing the angular view, and (F) SEM image of a cross section of the final device showing (a) 100 nm Ti film, (b) 50 nm protective thin film of Pt, (c) deposited FTO layer, and (d) thin film of $ZnFe_2O_4/\alpha$-Fe_2O_3 composite.

hydrocarbon originating from XPS instrument itself used as a standard. Figure 2b demonstrates the high-resolution XPS spectra of Fe 2p, which shows two splitting peaks of Fe ($2p_{1/2}$) and Fe ($2p_{3/2}$). The Fe 2p peaks for the ZF2 composite are positioned at binding energies of 711.3 and 724.9 eV, while these peaks for ZF1composite are located at the binding energies of 710.7 and 924.1 eV. The difference in binding energies of Fe 2p for both ZF1 and ZF2 composites is due to the difference between the ratio of $ZnFe_2O_4$ and α-Fe_2O_3 in these two composites. The binding energies of Fe 2p peaks in both the composites (ZF1 and ZF2) together with the presence of a satellite peak show that Fe is present only in the form of Fe^{3+} and there is no Fe^{2+} state in these composites[31−33] The peaks located at about 712 and 713.5 eV in XPS spectra of ZF1 and ZF2 composites, respectively, are attributed to Fe^{3+}, which is bonded with a hydroxyl group (−OH). The high-resolution XPS spectra of O 1s of ZF1 and ZF2 composites are shown in Figure 2C. The O 1s spectrum of ZF2 is divided into two distinct peaks: (a) a sharp peak with a high intensity at a binding energy of 529.9 eV, which is assigned to the metal−oxygen bonds; (b) a peak located at 531.2 eV, which is ascribed to hydroxyl group. The peaks positions at O 1s spectrum of ZF1 are slightly shifted to high binding energies. In fact, the metal−oxygen bonding in the ZF1 composite is shifted to 530.2 eV. The prominent shift is observed for the bonding between hydroxyl groups and Fe^{3+}. These shifts in the binding energies of O 1s spectra confirm the difference of the molar ratio of $ZnFe_2O_4$ and α-Fe_2O_3 in ZF1 and ZF2 composites. As shown in Figure 2D, the peaks located at 1044 and 1021 eV are attributed to Zn ($2p_{1/2}$) and Zn ($2p_{3/2}$) respectively.[34]

The quantitative studies of $ZnFe_2O_4/\alpha$-Fe_2O_3 composite thin films were performed by using X-ray fluorescence (XRF) spectrometry, and their results are shown in Figure 3 and Figure S1. The results of XRF tests confirm the molar ratios of ZF1, ZF2, and ZF3 composites are 1:1, 1:2, and 1:3, respectively.

The morphology of the $ZnFe_2O_4/\alpha$-Fe_2O_3 composite thin film deposited on FTO glass and 3D NSP are studied by scanning electron microscopy (SEM). Panels A−C of Figure 4 show the low- and high-resolution SEM images of $ZnFe_2O_4/\alpha$-Fe_2O_3 composite thin films deposited on FTO glass. As seen, the FTO glass is well-covered by the photoactive composite with an average grain size of 150 nm. Panels A and B of Figure 5 present the low- and high-resolution SEM images of 3D NSP samples. As illustrated, the spikes are well-aligned in a square shape with 1.2 μm pitch and 1 μm height. Figure 5C shows the SEM image of 3D NSP coated by uniform protective layers of Ti and Pt. Figure 5D shows the cross section of the 3D NSP sample with 100 and 50 nm thick films of Ti and Pt protective layers, respectively. The angular view the SEM image of a multilayered device after USP deposition is shown in Figure 5E. As shown, the $ZnFe_2O_4/\alpha$-Fe_2O_3 composite is uniformly deposited on 3D NSP and the distance between the edges of two adjacent spikes in the final multilayered device is 550 nm, which could allow better optical absorption of incident radiation of comparable wavelength. The cross-sectional SEM image of the multilayered device is shown in Figure 5F, which represents (a) a 100 nm thick protective layer of Ti, (b) a Pt layer with 50 nm thickness, (c) a 100 nm thick FTO film, and (d) the $ZnFe_2O_4/\alpha$-Fe_2O_3 composite thin film. Figure S2 shows the elemental mapping of Zn, Fe, O, Sn, Ti, Pt, and Al for $ZnFe_2O_4/\alpha$-Fe_2O_3 composite thin films, which have a uniform distribution through the layer. To study the light absorption properties of composites, UV−vis spectroscopic analyses of $ZnFe_2O_4/Fe_2O_3$ composites (deposited on FTO glass) and the pure hematite thin films (deposited on FTO glass) were performed (Supporting Information Figure S3). UV−vis measurements revealed that the absorbance decreases in the lower wavelength region with the increase in $ZnFe_2O_4$ contents in the composites, which is probably due to the smaller absorption of $ZnFe_2O_4$ than that of Fe_2O_3.[24] However, the absorbance at the higher wavelength region has increased with the increase in percentage of $ZnFe_2O_4$ in the composites.

Photoelectrochemical Study. The fabricated thin films were tested for PEC water oxidation reaction. The photocurrent density with respect to the applied potential (vs Ag/
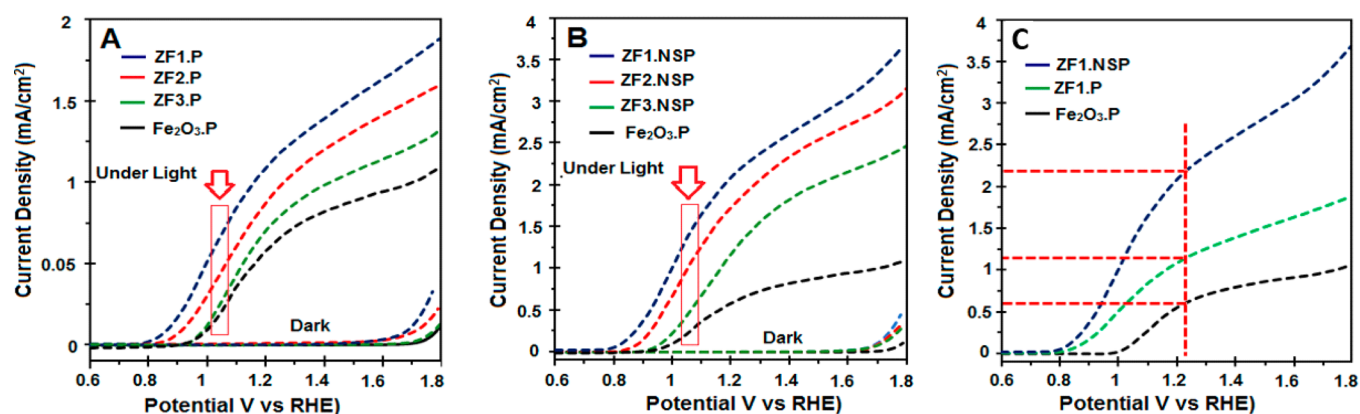
Figure 6. (A) Linear sweep voltammograms (LSV) of ZnFe$_2$O$_4$/Fe$_2$O$_3$ composites deposited on planar FTO-coated glass. (B) LSV curves of ZnFe$_2$O$_4$/Fe$_2$O$_3$ composites deposited on 3D nanospikes. (C) Comparison of photocurrent densities of planar and 3D nanostructure devices.
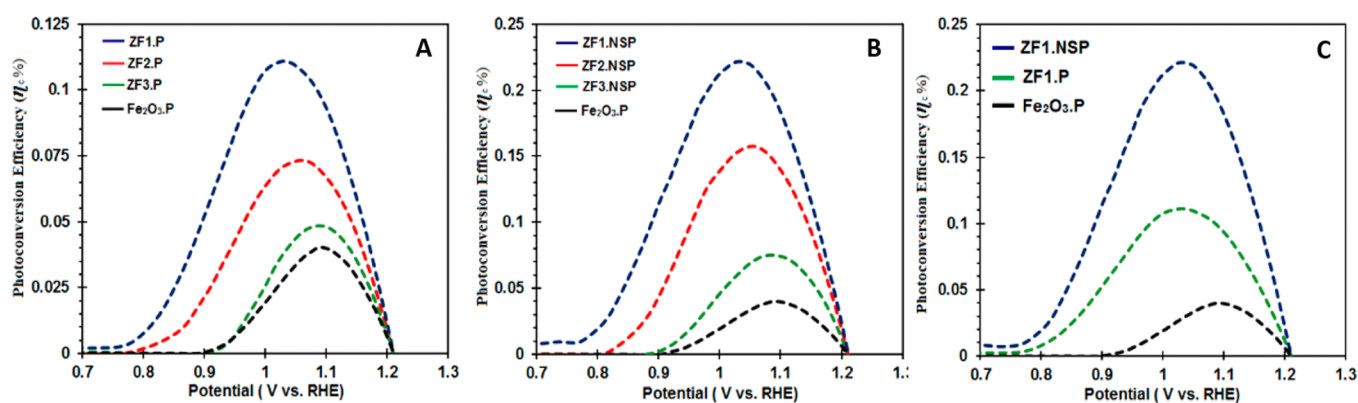
Figure 7. Plot of energy conversion efficiency (η_c) versus applied potential. The applied potential was calculated according to the equation, $E_{app} = E_{meas} - E_{ocp}$.

AgCl) was measured under the illumination of a solar simulator (AM 1.5, 100 mW/cm^2). Figure 6A shows the $J-V$ curves of ZnFe$_2$O$_4$/α-Fe$_2$O$_3$ composite films deposited on a planar substrate. The photocurrent density for composite film increases with the increase in percentage of ZnFe$_2$O$_4$ in the ZnFe$_2$O$_4$/α-Fe$_2$O$_3$ composite. The highest photocurrent density (1.14 mA/cm^2) at 1.23 V$_{RHE}$ is achieved for the planar device with a ratio of 1:1 for ZnFe$_2$O$_4$ and α-Fe$_2$O$_3$ (ZF1-P). This value is 1.81 times higher than that of pure hematite (0.63 mA/cm^2) deposited on the FTO glass. A further ramp in photocurrent density is observed with the increase in applied potential V$_{RHE}$ and a current of ca. 1.64 mA/cm^2 is obtained at 1.6 V$_{RHE}$ for the planar device (ZF1-P). It means that at 1.6 V$_{RHE}$, the photocurrent density of ZF1-P is 1.8 times higher than that of pure hematite for which the measured photocurrent density was 0.91 mA/cm^2 at the same applied voltage. The recorded values of photocurrent densities for other planar devices ZF2-P and ZF3-P are 0.94 and 0.76 mA/cm^2 at 1.23 V$_{RHE}$, respectively.

The $J-V$ curves of 3D NSP devices are shown in Figure 6B. It is clear that the photocurrent densities obtained from 3D NSP devices are much higher than those of planar devices. The photocurrent density of 2.19 mA/cm^2 is achieved from composite ZF1.NSP, which is 1.9 times higher than the value for the planar device with a similar composition (ZF1-P). When compared to the planar device of pure hematite, it is 3.4 times more active at 1.23 V$_{RHE}$ for the PEC water oxidation reaction. Upon a further increase of the potential to 1.6 V$_{RHE}$, the

photocurrent density of ZF1.NSP elevated to a value of 3 mA/cm^2. The photocurrent densities at 1.23 V$_{RHE}$ for other 3D NSP devices, namely, ZF2.NSP and ZF3.NSP, are recorded as 1.8 and 1.3 mA/cm^2, respectively.

The proper alignment of valence and conduction bands of ZnFe$_2$O$_4$ and α-Fe$_2$O$_3$ permits movement of electrons and holes at its interface, leading to better separation of photogenerated electrons and holes in ZnFe$_2$O$_4$/α-Fe$_2$O$_3$ composites as compared to the case of the pure hematite. The higher photocurrent densities of 3D NSP devices compared with those of the planar devices are due to larger surface areas and enhanced efficiency of optical absorption of 3D NSP devices.

To quantify the photoconversion efficiency (η_c), the following equation was used and the results are summarized in Figure 7 and Table 2.

$$\eta_c \, (\%) = \frac{J_p[(E^\circ_{rev} - |E_{app}|)]}{I(\text{light})} \times 100$$

where η_c is the photoconversion efficiency, J_p represents the current density under illumination, E°_{rev} denotes the standard reversible potential, which is equal to 1.23 V vs RHE, E_{app} is the potential applied across the electrodes ($E_{app} = E_{meas} - E_{ocp}$), E_{meas} represents the potential of working electrode vs Ag/AgCl, E_{ocp} represents the potential (vs Ag/AgCl) of working electrode under open circuit condition), and $I(\text{light})$ is the intensity of incident light which is equal to 100 mW/cm^2.

Table 2. Summary of the Results Extrapolated from the Photocurrent Density and PhotoConversion Efficiency

devices codes	type of device	composition $znfe_2o_4$:fe_2o_3	photocurrent density (mA/cm^2) at 1.23 V vs RHE	PCE (η_c %) at 1.23 V vs RHE
Fe_2O_3-P	planar	pure hematite	0.63	0.04
ZF1-P	planar	1:1	1.14	0.11
ZF2-P	planar	1:2	0.94	0.07
ZF3-P	planar	1:3	0.76	0.05
ZF1-NSP	3D nanostructured	1:1	2.19	0.22
ZF2-NSP	3D nanostructured	1:2	1.8	0.16
ZF3-NSP	3D nanostructured	1:3	1.3	0.075

At the applied potential of 1.23 V vs RHE, the maximum photoconversion efficiency among the planar devices is recorded as 0.11% for ZF1-P compared to results from other planar devices, i.e., ZF2-P and ZF3-P, for which the measured values of photoconversion efficiencies are 0.073 and 0.5%, respectively. This value of photoconversion efficiency is 2.75 times higher than that of pure hematite (η_c = 0.04%) at a similar applied voltage (1.23 V vs RHE).

Among the 3D NSP devices, the maximum value of photoconversion efficiency of 0.22% is achieved at 1.23 V vs RHE for ZF1.NSP. This value is 5.5 times larger than that of pure hematite deposited on FTO glass at the same conditions. The photoconversion efficiencies at 1.23 V vs RHE for other 3D NSP devices (ZF2.NSP and ZF3.NSP) are recorded as 0.16% and 0.075%, respectively.

Photoluminescence Studies. Photoluminescence (PL) tests were carried out to study the origin of high photoconversion efficiencies of $ZnFe_2O_4$/Fe_2O_3 composite photoanodes in PEC water oxidation as compared to results for the pure hematite photoanode. The photoluminescence peak is mainly the result of photogenerated charge recombination.[35−37] As shown in Figure 8, by an increase in the amount of $ZnFe_2O_4$ component in $ZnFe_2O_4$/Fe_2O_3 composite thin film, the PL intensity decreases. In fact, the lowest PL intensity was obtained for ZF1 in which the molar ratios of both components are equal. On the basis of the PL results, the efficient charge separation in $ZnFe_2O_4$/Fe_2O_3 composite thin films may be due
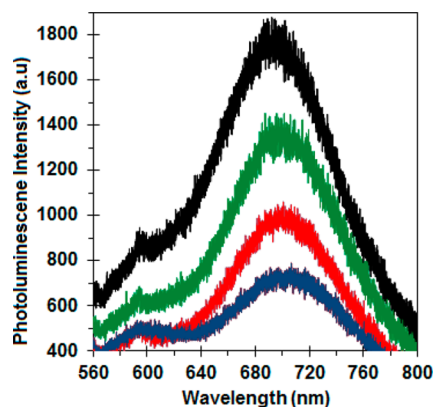
Figure 8. PL spectra of pure hematite (black), ZF3 (green), ZF2 (red), and ZF1 (blue).

to its higher activation in PEC water oxidation as compared to the case for pure hematite.

Charge Transfer Studies. To investigate the origin of enhanced performance of $ZnFe_2O_4$/α-Fe_2O_3 composite thin films with respect to bare α-Fe_2O_3, we performed a potentiostatic electrochemical impedance spectroscopy (EIS) test. The EIS measurements were performed at the applied voltage of 1.23 vs RHE in 1 M NaOH solution using single-compartment three-electrode systems with Ag/AgCl and platinum wire as reference and counter electrodes, respectively. The Nyquist impedance plots of photoanodes are shown in Figure 9. The experimental results were fitted to an equivalent
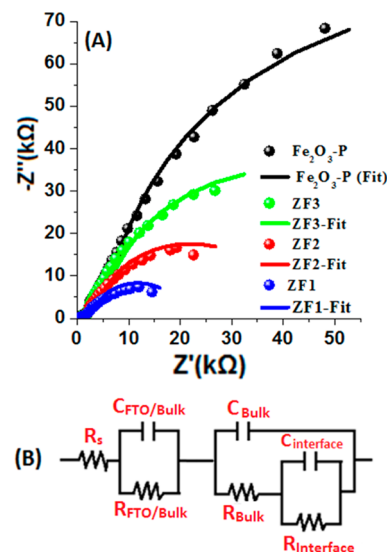
Figure 9. EIS of photoanodes in Nyquist plots in 1 M NaOH at a dc potential of 0.2 V vs Ag/AgCl with an ac potential frequency range from 100 0000 to 0.1 Hz.

randle circuit shown in the inset image of Figure 9. In this circuit model (RC), R_s represents the solution resistance, which is in a series of a parallel RC that models the FTO/semiconductor interface ($R_{FTO/bulk}$ and $C_{FTO/bulk}$). In the second RC circuit, R_{Bulk} is the charge transfer resistance inside the semiconductor and C_{Bulk} presents the space charge region of semiconductor whereas $R_{Interface}$ and $C_{Interface}$ are the charge transfer resistances across the semiconductor/electrolyte interface and double-layered capacitance relative to the semiconductor/electrolyte interface, respectively. The resistance values relative to semiconductor/electrolyte interface ($R_{interface}$) are much larger than R_{Bulk} for all electrodes, confirming that the charge transfer resistance at the semiconductor/electrolyte interface is the limiting process and it controls the overall water oxidation reaction that takes place at the electrode surface.[38−42] As shown in Table 3, the values of $R_{interface}$ for $ZnFe_2O_4$/α-Fe_2O_3 composites are lowered as compared to that of pure α-Fe_2O_3 and there is a decreasing trend in the values of $R_{interface}$ with the increasing $ZnFe_2O_4$ component in $ZnFe_2O_4$/α-Fe_2O_3 composites and the reduction effect becomes more pronounced in ZF1-P ($R_{interface}$ is reduced 9 times compared to that for the pure hematite photoanode (α-Fe_2O_3-P)). The reduction in $R_{interface}$ reveals that the charge transfer across the semiconductor/electrolyte interface is significantly promoted by coupling α-Fe_2O_3 with $ZnFe_2O_4$ and thus electron−hole recombination is greatly suppressed.[42] The lowest value of $R_{interface}$ (16.39 kΩ) was obtained for ZF1 (having an equal

Table 3. Resistance and CPE Values of the Corresponding Models

	R_s	$R_{FTO/Bulk}$ (kΩ) and $C_{FTO/Bulk}$ (μF)	R_{Bulk} (kΩ) and C_{Bulk} (μF)	$R_{interface}$ (kΩ) and $C_{interface}$ (μF)
Fe$_2$O$_3$-P	0.605	6.224	1.580	147.050
		4.1845×10^{-3}	2.15×10^{-2}	3.532×10^{-3}
ZF3-P	0.607	4.537	1.229	69.575
		1.262×10^{-2}	2.73×10^{-2}	1.673×10^{-2}
ZF2-P	0.600	3.127	1.072	34.790
		1.529×10^{-2}	3.8×10^{-2}	1.968×10^{-2}
ZF1-P	0.558	2.236	0.974	16.390
		1.664×10^{-2}	3.79×10^{-2}	3.192×10^{-2}

molar ratio of ZnFe$_2$O$_4$ and α-Fe$_2$O$_3$) and it agrees with the highest photocurrent density of the ZF1 photoelectrode during LSV measurements. Moreover, the charge conductivities of ZnFe$_2$O$_4$/α-Fe$_2$O$_3$ composite thin films are larger than the charge conductivity of the bare α-Fe$_2$O$_3$ thin film (1580 Ω). The increase in charge conductivity with an increase of ZnFe$_2$O$_4$ contributes to the higher PEC activity of the ZnFe$_2$O$_4$/α-Fe$_2$O$_3$ composite compared to that of bare α-Fe$_2$O$_3$. Similarly, the charge transfer resistances across FTO/ZnFe$_2$O$_4$/α-Fe$_2$O$_3$ interfaces have lower values (FTO/ZF1 interface with lowest charge transfer resistance of 2236 Ω) than the FTO/α-Fe$_2$O$_3$ interface (6224 Ω). This confirms that the movement of charge is comparatively faster through FTO/(ZnFe$_2$O$_4$/α-Fe$_2$O$_3$) interface than through the FTO/α-Fe$_2$O$_3$ interface.

In conclusion, the higher PEC activities of ZnFe$_2$O$_4$/α-Fe$_2$O$_3$ composite thin films relative to that of the bare α-Fe$_2$O$_3$ thin film was due to the pronounced charge mobility across all possible interfaces (FTO/semiconductor/electrolyte). Furthermore, the charge transfer resistance across the semiconductor/electrolyte interface was the controlling factor of the overall water-splitting reaction that takes place at the electrode surface. Therefore, the highest PEC activity of ZF1 is attributed to the lowest charge transfer resistance across the ZF1/electrolyte interface that dramatically suppressed the electron–hole recombination.

CONCLUSIONS

The ZnFe$_2$O$_4$/α-Fe$_2$O$_3$ composite thin films with different molar ratios are successfully deposited on planar fluorine-doped tin oxide (FTO) glass as well as 3D nanospikes (NSP). The structural, compositional, and morphological studies are carried out by using many techniques including powder X-ray diffraction (PXRD), X-ray photoelectronic spectroscopy (XPS), X-ray fluorescence (XRF) spectrometry, scanning electron microscopy (SEM), etc. It has been found that the ZnFe$_2$O$_4$/α-Fe$_2$O$_3$ composite materials are more active for photoelectrochemical water oxidation than bare α-Fe$_2$O$_3$. The higher activity of ZnFe$_2$O$_4$/α-Fe$_2$O$_3$ composite thin films is attributed to better separation of photogenerated electrons and holes. The composite ZF1 with an equal molar ratio of ZnFe$_2$O$_4$ and α-Fe$_2$O$_3$ shows the best performance in photoelectrochemical (PEC) water oxidation. The electrochemical impedance spectroscopy (EIS) test shows that the charge conductivity of the ZnFe$_2$O$_4$/α-Fe$_2$O$_3$ composites is much higher than that of pure α-Fe$_2$O$_3$. The reduction in charge transferred resistance values across all possible interfaces is observed in ZnFe$_2$O$_4$/α-Fe$_2$O$_3$ composites as compared to

the case of pure α-Fe$_2$O$_3$. It is concluded that composite ZF1 has the highest charge conductivity and highest activity in photoelectrochemical water splitting. The performance of a synthesized photoanode was further enhanced by using 3D NSP substrates due to larger surface area and effective light-trapping properties.

ASSOCIATED CONTENT

Ⓢ Supporting Information

The Supporting Information is available free of charge on the ACS Publications website at DOI: 10.1021/acs.jpcc.7b05266.

XRF, EDS, and UV−vis spectroscopic analysis, SEM images, and molar concentrations (PDF)

AUTHOR INFORMATION

Corresponding Authors
*Zhiyong Fan. E-mail: eezfan@ust.hk.
*Muhammad Arif Nadeem. E-mail: manadeem@qau.edu.pk. Phone: +92-51-9064-2062.

ORCID Ⓘ
Aashir Waleed: 0000-0002-6929-8373
Mohammad Mahdi Tavakoli: 0000-0002-8393-6028
Zhiyong Fan: 0000-0002-5397-0129
Muhammad Arif Nadeem: 0000-0003-0738-9349

Notes
The authors declare no competing financial interest.

REFERENCES

(1) Qiu, Y.; Leung, S. F.; Wei, Z.; Lin, Q.; Zheng, X.; Zhang, Y.; Fan, Z.; Yang, S. Enhanced Charge Collection for Splitting of Water Enabled by an Engineered Three-Dimensional Nanospike array. *J. Phys. Chem. C* **2014**, *118*, 22465−22472.
(2) Qiu, Y.; Leung, S. F.; Zhang, Q.; Hua, B.; Lin, Q.; Wei, Z.; Tsui, K. H.; Zhang, Y.; Yang, S.; Fan, Z. Efficient Photoelectrochemical Water Splitting with Ultrathin Films of Hematite on Three Dimensional Nanophotonic Structures. *Nano Lett.* **2014**, *14*, 2123−2129.
(3) Nocera, D. G. The Artificial Leaf. *Acc. Chem. Res.* **2012**, *45*, 767−776.
(4) Walter, M. G.; Warren, E. L.; McKone, J. R.; Boettcher, S. W.; Mi, Q.; Santori, E. A.; Lewis, N. S. Solar Water Splitting Cells. *Chem. Rev.* **2010**, *110*, 6446−6473.
(5) Joya, K. S.; Joya, Y. F.; Ocakoglu, K.; van de Krol, R. Water-Splitting Catalysis and Solar Fuel Devices: Artificial Leaves on the Move. *Angew. Chem., Int. Ed.* **2013**, *52*, 10426−10437.
(6) Lee, M. H.; Takei, K.; Zhang, J.; Kapadia, R.; Zheng, M.; Chen, Y.; Nah, J.; Matthews, T. S.; Chueh, Y.; Ager, J. W. p-Type InP Nanopillar Photocathodes for Efficient Solar-Driven Hydrogen Production. *Angew. Chem.* **2012**, *124*, 10918−10922.
(7) Hoffmann, M. R.; Martin, S. T.; Choi, W.; Bahnemann, D. W. Environmental Applications of Semiconductor Photocatalysis. *Chem. Rev.* **1995**, *95*, 69−96.
(8) Silva, C. G.; Juarez, R.; Marino, T.; Molinari, R.; García, H. Influence of Excitation Wavelength (UV or Visible Light) on the Photocatalytic Activity of Titania Containing Gold Nanoparticles for

the Generation of Hydrogen or Oxygen from Water. *J. Am. Chem. Soc.* **2011**, *133*, 595−602.

(9) Luo, J.; Tilley, S. D.; Steier, L.; Schreier, M.; Mayer, M. T.; Fan, H. J.; Gratzel, M. Solution Transformation of Cu_2O into $CuInS_2$ for Solar Water Splitting. *Nano Lett.* **2015**, *15*, 1395−1402.

(10) Li, Z.; Wang, F.; Kvit, A.; Wang, X. Nitrogen Doped 3D Titanium Dioxide Nanorods Architecture with Significantly Enhanced Visible Light Photoactivity. *J. Phys. Chem. C* **2015**, *119*, 4397−4405.

(11) Chen, H. M.; Chen, C. K.; Liu, R. S.; Zhang, L.; Zhang, J.; Wilkinson, D. P.Nano-Architecture and Material Designs for Water Splitting Photoelectrodes. *Chem. Soc. Rev.* **2012**, *41*, 5654−5671.

(12) Chen, X.; Shen, S.; Guo, L.; Mao, S. S. Semiconductor-Based Photocatalytic Hydrogen Generation. *Chem. Rev.* **2010**, *110*, 6503−6570.

(13) Yu, Q.; Meng, X.; Wang, T.; Li, P.; Ye, J. Hematite Films Decorated with Nanostructured Ferric Oxyhydroxide as Photoanodes for Efficient and Stable Photoelectrochemical Water Splitting. *Adv. Funct. Mater.* **2015**, *25*, 2686−2692.

(14) Deng, J.; Lv, X.; Liu, J.; Zhang, H.; Nie, K.; Hong, C.; Wang, J.; Sun, X.; Zhong, J.; Lee, S. T. L. Thin-Layer Fe2TiO5 on Hematite for Efficient Solar Water Oxidation. *ACS Nano* **2015**, *9*, 5348−5356.

(15) Tilley, S. D.; Cornuz, M.; Sivula, K.; Grätzel, M. Angew. Light-Induced Water Splitting with Hematite: Improved Nanostructure and Iridium Oxide Catalysis. *Angew. Chem., Int. Ed.* **2010**, *49*, 6405−6408.

(16) Cummings, C. Y.; Marken, F.; Peter, L. M.; Wijayantha, K. G. U.; Tahir, A. A. New Insights into Water Splitting at Mesoporous α-Fe_2O_3 Films: A Study by Modulated Transmittance and Impedance Spectroscopies. *J. Am. Chem. Soc.* **2012**, *134*, 1228−1234.

(17) Glasscock, J. A.; Barnes, P. R. F.; Plumb, I. C.; Savvides, N. Enhancement of Photoelectrochemical Hydrogen Production from Hematite Thin Films by the Introduction of Ti and Si. *J. Phys. Chem. C* **2007**, *111*, 16477−16488.

(18) Sartoretti, C. J.; Alexander, B. D.; Solarska, R.; Rutkowska, I. A.; Augustynski, J. Photoelectrochemical Oxidation of Water at Transparent Ferric Oxide Film Electrodes. *J. Phys. Chem. B* **2005**, *109*, 13685−13692.

(19) Li, F.; Wang, H.; Wang, L.; Wang, J. Magnetic Properties of $ZnFe_2O_4$ Nanoparticles Produced by a Low-Temperature Solid-State Reaction Method. *J. Magn. Magn. Mater.* **2007**, *309*, 295−299.

(20) Ponpandian, N.; Narayanasamy, A. Influence of Grain Size and Structural Changes on the Electrical Properties of Nanocrystalline Zinc Ferrite. *J. Appl. Phys.* **2002**, *92*, 2770−2778.

(21) Yin, J.; Bie, L. J.; Yuan, Z. H. Photoelectrochemical Property of $ZnFe_2O_4/TiO_2$ Double-Layered Films. *Mater. Res. Bull.* **2007**, *42*, 1402−1406.

(22) McDonald, K. J.; Choi, K. S. Synthesis and Photoelectrochemical Properties of $Fe_2O_3/ZnFe_2O_4$ Composite Photoanodes for Use in Solar Water Oxidation. *Chem. Mater.* **2011**, *23*, 4863−4869.

(23) Miao, C.; Ji, S.; Xu, G.; Liu, G.; Zhang, L.; Ye, C. Micro-Nano-Structured Fe_2O_3:Ti/$ZnFe_2O_4$ Heterojunction Films for Water Oxidation. *ACS Appl. Mater. Interfaces* **2012**, *4*, 4428−4433.

(24) Liu, Q.; Cao, F.; Wu, F.; Tian, W.; Li, L. Interface Reacted $ZnFe_2O_4$ on α-Fe_2O_3 Nanoarrays for Largely Improved Photoelectrochemical Activity. *RSC Adv.* **2015**, *5*, 79440−79446.

(25) Luo, Z.; Li, C.; Zhang, D.; Wang, T.; Gong, J. Highly-Oriented $Fe_2O_3/ZnFe_2O_4$ Nanocolumnar Heterojunction with Improved Charge Separation for Photoelectrochemical Water Oxidation. *Chem. Commun.* **2016**, *52*, 9013−9015.

(26) Pinaud, B. A.; Chen, Z.; Abram, D. N.; Jaramillo, T. F. Thin Films of Sodium Birnessite-Type MnO_2: Optical Properties, Electronic Band Structure, and Solar Photoelectrochemistry. *J. Phys. Chem. C* **2011**, *115*, 11830−11838.

(27) Hussain, S.; Hussain, S.; Waleed, A.; Tavakoli, M. M.; Wang, Z.; Yang, S.; Fan, Z.; Nadeem, M. A. Fabrication of $CuFe_2O_4$/α-Fe_2O_3 Composite Thin Films on FTO Coated Glass and 3-D Nanospike Structures for Efficient Photoelectrochemical Water Splitting. *ACS Appl. Mater. Interfaces* **2016**, *8*, 35315−35322.

(28) Waleed, A.; Tavakoli, M. M.; Gu, L.; Wang, Z.; Zhang, D.; Manikandan, A.; Zhang, Q.; Zhang, R. J.; Chueh, Y. L.; Fan, Z. Lead-Free Perovskite Nanowire Array Photodetectors with Drastically Improved Stability in Nanoengineering Templates. *Nano Lett.* **2017**, *17*, 523.

(29) Waleed, A.; Tavakoli, M. M.; Gu, L.; Hussain, S.; Zhang, D.; Poddar, S.; Wang, Z.; Zhang, R.-J.; Fan, Z. All Inorganic Cesium Lead Iodide Perovskite Nanowires with Stabilized Cubic Phase at Room Temperature and Nanowire Array-based Photodetectors. *Nano Lett.* **2017**, *17*, 4951−4957.

(30) Waleed, A.; Zhang, Q.; Tavakoli, M. M.; Leung, S.; Gu, L.; He, J.; Mo, X.; Fan, Z. Performance improvement of solution-processed CdS/CdTe solar cells with a thin compact TiO2 buffer layer. *Sci. Bull.* **2016**, *61* (1), 86−91.

(31) Miao, C.; Ji, S.; Xu, G.; Liu, G.; Zhang, L.; Ye, Changhui. Micro-Nano-Structured Fe_2O_3: Ti/$ZnFe_2O_4$ Heterojunction Films for Water Oxidation. *ACS Appl. Mater. Interfaces* **2012**, *4*, 4428−4433.

(32) Guo, Y.; Fu, Y.; Liu, Y.; Shen, S. Photoelectrochemical Activity of $ZnFe_2O_4$ Modified α-Fe_2O_3 Nanorod Array Films. *RSC Adv.* **2014**, *4*, 36967−36972.

(33) Wang, M.; Sun, L.; Cai, J.; Huang, P.; Su, Y.; Lin, C. A Facile Hydrothermal Deposition of $ZnFe_2O_4$ Nanoparticles on TiO_2 Nanotube Arrays for Enhanced Visible Light Photocatalytic Activity. *J. Mater. Chem. A* **2013**, *1*, 12082−12087.

(34) NuLi, Y. N.; Chu, Y. Q.; Qin, Q. Z. Nanocrystalline $ZnFe_2O_4$ and Ag-Doped $ZnFe_2O_4$ Films Used as New Anode Materials for Li-Ion Batteries. *J. Electrochem. Soc.* **2004**, *151*, A1077−A1083.

(35) Shen, S.; Jiang, J.; Guo, P.; Kronawitter, C. X.; Mao, S. S.; Guo, L. Effect of Cr Doping on the Photoelectrochemical Performance of Hematite Nanorod Photoanodes. *Nano Energy* **2012**, *1*, 732−741.

(36) Ilyas, U.; Rawat, R. S.; Roshan, G.; Tan, T. L.; Lee, P.; Springham, S. V.; Zhang, S.; Fengji, Li.; Chen, R.; Sun, H. D. Quenching of Surface Traps in Mn Doped ZnO Thin Films for Enhanced Optical Transparency. *Appl. Surf. Sci.* **2011**, *258*, 890−897.

(37) Luo, J.; Ma, L.; He, T.; Ng, C. F.; Wang, S.; Sun, H.; Fan, H. J. TiO2/(CdS, CdSe, CdSeS) Nanorod Heterostructures and Photoelectrochemical Properties. *J. Phys. Chem. C* **2012**, *116*, 11956−11963.

(38) Malara, F.; Minguzzi, A.; Marelli, M.; Morand, S.; Psaro, R.; Santo, V. D.; Naldoni, A. α-Fe_2O_3/NiOOH: An Effective Heterostructure for Photoelectrochemical Water Oxidation. *ACS Catal.* **2015**, *5*, 5292−5300.

(39) Tahir, A. A.; Wijayantha, K. G. U.; Yarahmadi, S. S.; Mazhar, M.; McKee, V. Nanostructured α-Fe_2O_3 Thin Films for Photoelectrochemical Hydrogen Generation. *Chem. Mater.* **2009**, *21*, 3763−3772.

(40) Zhang, W.-D.; Jiang, L.-C.; Ye, J.-S. Photoelectrochemical Study on Charge Transfer Properties of ZnO Nanowires Promoted by Carbon Nanotubes. *J. Phys. Chem. C* **2009**, *113*, 16247−16253.

(41) Xie, Y.; Zhou, L.; Lu, J. Photoelectrochemical Behavior of Titania Nanotube Array Grown on Nanocrystalline Titanium. *J. Mater. Sci.* **2009**, *44*, 2907−2915.

(42) Song, X. M.; Wu, J. M.; Tang, M. Z.; Qi, B.; Yan, M. Enhanced Photoelectrochemical Response of a Composite Titania Thin Film with Single-Crystalline Rutile Nanorods Embedded in Anatase Aggregates. *J. Phys. Chem. C* **2008**, *112*, 19484−19492.